Research paper

Quantification of numerical uncertainties of CFD-predicted wind turbine performance with overset grids

Maokun Ye [a], Yan Zhao [b], Hamn-Ching Chen [c], Decheng Wan [a],*

[a] Computational Marine Hydrodynamics Lab (CMHL), School of Naval Architecture, Ocean and Civil Engineering, Shanghai Jiao Tong University, Shanghai, China
[b] Key Laboratory of Far-shore Wind Power Technology of Zhejiang Province, Huadong Engineering Corporation Limited, Hangzhou, China
[c] Zachry Department of Civil & Environmental Engineering, Texas A&M University, College Station, TX, USA

ARTICLE INFO

ABSTRACT

The overset-grid technique is supposed to be the most theoretically correct and powerful approach to be used in the Computational Fluid Dynamics (CFD) simulations of wind turbines. The results obtained by CFD simulations which leverage the overset-grid technique could be sensitive to many numerical configurations, e.g., grid spacing, time increment, and turbulence models, etc. As a result, it is important to systematically quantify numerical uncertainties in order to obtain trustworthy predictions from these simulations. In this paper, the performance characteristics of the wind turbine tested in the Norwegian University of Science and Technology (NTNU) Blind Test (BT) 1 experiment is analyzed by using the CFD code Finite-Analytic Navier-Stokes (FANS) with overset grids, and a thorough verification study aiming at quantifying the numerical uncertainties in the CFD predictions is performed. First, the CFD approach adopted and the verification method leveraged in the present work are introduced. Next, the wing tunnel tests of the S826 wing section and the NTNU BT1 wind turbine are described in detail. First, as a benchmark, CFD simulations using the FANS code with overset grids are performed targeting a wing section of S826 airfoil before we move to full turbine simulations. Comparison of the predicted surface pressure with the measurement is performed and a good agreement is observed. Then, CFD simulations are performed for the full turbine of BT1. In order to assess the numerical uncertainties relating to the spatial and temporal discretization errors, a numerical database obtained by using six different configurations of grid spacing and time increment is created. In each of the computational grids, the details of the wind turbine's geometry are precisely captured by taking the advantage of overset grids. Unsteady Reynolds.

Averaged Navier-Stokes (URANS) simulations with a two-layer $k - \epsilon$ turbulence model are performed. The rotation of the rotor is achieved by moving the according overset-grid blocks.

Through the utilization of a contemporary verification analysis for the numerical predictions, the numerical uncertainties stem from discretization errors in the computed thrust (C_T) and power (C_P) coefficients are evaluated. Finally, CFD calculations are conducted for different Tip-Speed Ratios (TSRs), and the CFD results are compared to the experimental data.

1. Introduction

Over the last few years, Computational Fluid Dynamics (CFD) approaches of varying complexity and precision have been extensively utilized in wind energy research and industrial applications, emerging as a robust tool for analyzing wind turbine aerodynamics. Two main categories of methods are available based on how wind turbine geometries are handled in CFD simulations: the Blade Element Method (BEM) based methods and the Fully-Resolved Geometry (FRG) methods.

In CFD simulations employing BEM-based methods such as the actuator disc (AD) method (Sørensen and Myken, 1992; Nilsson, 2015; de Jong Helvig et al., 2021) and the actuator line (AL) method (Sorensen and Shen, 2002; Shen et al., 2005; Troldborg, 2009), the effects of wind turbine blades are simplified as equivalent forces in the fluid field. This simplification allows for the avoidance of challenges associated with resolving blade geometries and wall boundary layers (Troldborg, 2009). Afterward, the simplified turbine models are integrated into Reynolds-Averaged Navier-Stokes (RANS) and Large Eddy Simulation (LES) solvers (Breton et al., 2017; Thé and Yu, 2017) to compute the turbine generated wake. As the forces on the wind turbine blades are

---

* Corresponding author.
  E-mail address: dcwan@sjtu.edu.cn (D. Wan).

typically prescribed in this approach, often through the use of look-up tables, these simulations are primarily aimed at effectively resolving the wake generated by the turbine (Feliciano et al., 2018; Draper et al., 2018; Tian et al., 2021; Zhang et al., 2022; Ghandour et al., 2022). Moreover, this methodology has been applied in investigating flow phenomena within wind farms (Calaf et al., 2010; Nilsson et al., 2015) and the interaction between wind turbine wakes and the atmospheric boundary layers (Xie and Archer, 2017; Bouras et al., 2018).

However, this methodology may be subject to scrutiny as it commonly assumes two-dimensional flow on the blade surfaces, a representation that may not align with real-world physical conditions (Duque et al., 1999; Plaza et al., 2015). In the case of floating offshore wind turbines (FOWTs), the turbines undergo an additional six-degrees-of-freedom (6-DoF) motion, resulting in highly unsteady and three-dimensional airflow around the blades. Consequently, the fundamental assumptions of BEM-based methods could be compromised, potentially leading to inaccuracies in predicting aerodynamic forces on FOWTs. Subsequently, such inaccuracies can impact the precision of platform response predictions and, ultimately, the wakes generated by the FOWTs. To summarize, obtaining a comprehensive comprehension of the flow near the blades is of significant importance for accurately predicting wind turbine performance, platform response, and the wakes produced by FOWTs.

In recent years, the increased affordability of computational resources has led to a more frequent application of Fully-Resolved Geometry (FRG) in CFD simulations of wind turbines, representing the most theoretically sound approach for such calculations. This method necessitates the use of either a sliding interface or an overset-grid technique to manage the relative motion between the wind turbine rotor (comprising the blades and hub) and other stationary components, such as the tower, in the simulations. The utilization of FRG is particularly advantageous for simulating FOWTs due to its capability to accurately capture the unsteady three-dimensional flow around the blades without simplification. This capability enables a precise analysis of FOWT aerodynamics in ocean environment, including the influence of waves and wind, thereby contributing significantly to the understanding of the complex interactions between the wind turbine and the environment.

The sliding-interface technique is the first method employed to address the relative motion between the rotor and the stationary components. In the context of these simulations (Choi et al., 2013; Mo et al., 2013; Ye et al., 2023a; Xie and Archer, 2017), two distinct grids are typically generated: the inner grid and the outer grid. The rotation of the rotor is achieved by rotating the inner grid, which encompasses the rotor geometries. While these two grids are disconnected and can be individually generated, they should be closely attached but not overlapped (Liu et al., 2017). Flow information in the two grids is exchanged through the interface by extrapolation of variables. An inherent limitation of this approach is its ability to solely manage rotational motions, such as roll, pitch, and yaw. Consequently, when conducting CFD simulations of FOWTs, where all 6-DoF motions exist, specific treatment (Liu et al., 2017; Liu and Xiao, 2019; Fang et al., 2020) is essential to address the three translational motions: surge, sway, and heave. In contrast to the sliding-interface technique, the overset-grid approach provides greater flexibility in the CFD simulations of FOWTs (Zahle et al., 2009; Li et al., 2012; Lynch and Smith, 2013). Within these simulations, individual grid blocks are generated to encompass components such as the blades, nacelle, and tower, and these blocks are subsequently embedded within the background grids. Flow information between the overlapped grids is exchanged through variable interpolation, and each of the overset grids can theoretically move arbitrarily, rendering it the most suitable and promising approach for CFD simulations of FOWTs (Tran and Kim, 2016a, 2016b).

The establishment of credibility in CFD predictions is crucial before applying CFD methods to complex flow problems (Make and Vaz, 2015). For example, a comprehensive sensitivity analysis of numerical

configurations for CFD simulations of the MARIN Stock Wind Turbine (MSWT) was conducted by Make and Vaz (2015). Their study involved conducting steady CFD simulations to assess the impact of multiple numerical configurations, e.g., domain size, on the CFD predictions. Similarly, Wang et al. (2019) conducted a contemporary verification study for CFD simulations of a semi-submersible FOWT floater under pitch decay. They subsequently extended this approach to FOWT floater simulations under regular waves (Wang et al., 2021b), and considered the effect of mooring lines in a systematic V&V study (Wang et al., 2021a). In the context of CFD simulations employing the sliding-interface and overset-grid techniques, where flow information is exchanged among different grid blocks through extrapolation or interpolation, meticulous attention is required to address numerical uncertainties related to spatial and temporal sizes used in the calculations. Ye et al. (2023b) utilized a modern verification study to quantify numerical uncertainties in CFD-predicted turbine performance, determining that torque predictions are more sensitive to grid resolution than thrust. This methodology was also applied to assess wake characteristics of the same wind turbine (Ye et al., 2022, 2023a), with the relative motion between the rotor and the tower achieved using the sliding-interface technique. However, for CFD simulations using the overset-grid technique, previous studies primarily compared CFD results with experimental data, with absent, or at least limited, rigorous assessments of numerical uncertainties.

The goal of the present work is to establish a systematic and accessible procedure for obtaining reliable numerically predicted turbine performance from CFD simulations using overset grids. The remaining part of this paper is organized as follows. First, the CFD methods and techniques and the adopted verification procedure are introduced, and the wind tunnel tests for the S826 airfoil wing section and the NTNU BT1 wind turbine are then described. Afterward, as a benchmark case, CFD simulations adopting the overset-set grid technique for the S826 airfoil at various Angles of Attack (*AoA*) are performed before we jump into the NTNU BT1 turbine. Next, a numerical database obtained by using six different configurations of grid spacing and time increment is obtained by performing CFD simulations using FANS. Further, the adopted verification procedure is applied to the CFD-predicted turbine performance and to assess the numerical uncertainties in the CFD prediction relating to the discretization errors. That numerical uncertainty is then taken into consideration in the comparisons between the CFD predictions and the experimental measurements across a range of Tip-Speed Ratios (TSRs). Finally, conclusions are drawn based on the results and discussions.

2. Methodologies

In this section, the theories and techniques adopted in the CFD simulations performed in this study will be introduced, and the adopted verification procedure will be described in detail.

2.1. Numerical approach

2.1.1. Governing equations

The governing equations of fluids are the Navier-Stokes equations. Depending on the scales of turbulence that are resolved in the simulations, the Navier-Stokes equations can be solved by means of RANS, LES, or Direct Numerical Simulation (DNS). In the current study, the unsteady RANS equations are solved by using the FANS code:

$$\frac{\partial U_i}{\partial x_i} = 0 \tag{1}$$

$$\frac{\partial U_i}{\partial t} + U_j \frac{\partial U_i}{\partial x_j} = f_i + \frac{\partial}{\partial x_j} \left(-\frac{p}{\rho}\delta_{ij} + 2\nu S_{ij} - \langle u_i u_j \rangle \right) \tag{2}$$

where U_i is the mean velocity, u_i the fluctuating velocity, t the time, ρ the

fluid density (constant for incompressible flows), p the mean pressure, f_i the external force, and v is the kinematic viscosity. S_{ij} is the mean strain rate tensor, and it is defined as $S_{ij} = \frac{1}{2}\left(\frac{\partial U_i}{\partial x_j} + \frac{\partial U_j}{\partial x_i}\right)$. The term $\langle u_i u_j \rangle$, is the so-called Reynolds stress and is approximated by the following equation according to the well-known Boussinesq's eddy viscosity assumption:

$$-\langle u_i u_j \rangle = v_t \left(\frac{\partial U_i}{\partial x_j} + \frac{\partial U_j}{\partial x_i}\right) - \frac{2}{3} k \delta_{ij} \tag{3}$$

where v_t is the turbulent viscosity, or eddy viscosity, and it is computed by solving additional two turbulence transport equations in isotropic turbulence models, i.e. the turbulent kinetic energy k and the turbulent dissipation ε in the current study.

2.1.2. Turbulence closure

A two-layer $k - \epsilon$ model proposed by Chen and Patel (1988) is adopted for the turbulence closure in the current study. In the outer layer which is not closed to the wall, the standard $k - \epsilon$ turbulence model (Launder and Sharma, 1974; Launder and Spalding, 1983) is used.

$$\frac{\partial k}{\partial t} + U_j \frac{\partial k}{\partial x_j} = P_k - \epsilon + \frac{\partial}{\partial x_j}\left[\left(v + \frac{v_t}{\sigma_k}\right)\frac{\partial k}{\partial x_j}\right] \tag{4}$$

$$\frac{\partial \epsilon}{\partial t} + U_j \frac{\partial \epsilon}{\partial x_j} = C_{\epsilon 1}\frac{\epsilon}{k}\tau_{ij}\frac{\partial U_i}{\partial x_j} - C_{\epsilon 2}\frac{\epsilon^2}{k} + \frac{\partial}{\partial x_j}\left[\left(v + \frac{v_t}{\sigma_\epsilon}\right)\frac{\partial \epsilon}{\partial x_j}\right] \tag{5}$$

where P_k is the production rate of turbulent kinetic energy:

$$P_k = \tau_{ij}\frac{\partial U_i}{\partial x_j} = v_t \left(\frac{\partial U_i}{\partial x_j} + \frac{\partial U_j}{\partial x_i}\right)\frac{\partial U_i}{\partial x_j} \tag{6}$$

and the values of the closure constants are $C_{\epsilon 1} = 1.44, C_{\epsilon 2} = 1.92, C_\mu = 0.09, \sigma_k = 1.0, \sigma_\epsilon = 1.3$.

An algebraic relation is specified for the energy dissipation rate ε in the inner region of the boundary layer as:

$$\epsilon = \frac{k^{3/2}}{l_\epsilon} \tag{7}$$

and the eddy-viscosity is given by:

$$v_t = C_\mu \sqrt{k} l_\mu \tag{8}$$

In Eqs. (7) and (8), l_ϵ and l_μ represent the length scales of ϵ and v_t respectively, and is defined by the following relations:

$$l_\epsilon = C_l y \left[1 - \exp\left(\frac{-R_y}{A_\epsilon}\right)\right] \tag{9}$$

and

$$l_\mu = C_l y \left[1 - \exp\left(\frac{-R_y}{A_\mu}\right)\right] \tag{10}$$

where R_y is the turbulence Reynolds number defined by:

$$R_y = \frac{\sqrt{k}y}{v} \tag{11}$$

In the above expressions, the constant C_l is defined as $C_l = \kappa C_\mu^{-3/4}$ where κ is the von Karman constant. This approach guarantees a seamless distribution of eddy-viscosity at the interface connecting the two neighboring regions, i.e. inner and outer. The value of A_μ is calibrated to be 70, which recovers the log-law constant $B = 5.45$. Additionally, $A_\epsilon = 2C_l$ is set to maintain the appropriate asymptotic behavior of ϵ, such that $\epsilon = 2vk/y^2$, in the viscous sublayer.

2.1.3. The finite-analytic Navier-Stokes (FANS) code

In this study, we performed CFD simulations using the FANS code, which utilizes the Finite-Analytic method to solve the unsteady incompressible Navier-Stokes equations (Chen and Chen, 1984; Chen et al., 1990; Pontaza et al., 2005). FANS is capable of solving RANS or LES equations by using arbitrary configurations of overset grids. To handle complex configurations and flow conditions efficiently, the computational domain was divided into smaller overset grid blocks. The RANS or LES equations are then solved in a general curvilinear, body-fitted coordinate system for each of the overset grid blocks by utilizing the finite-analytic method, and the interpolation between different overset blocks is achieved by Lagrange interpolation at the fringes. The coupling of pressure and velocity to maintain fluid incompressibility is accomplished by leveraging a hybrid algorithm (Chen, 1989; Pontaza et al., 2005) that combines the Pressure Implicit with Split Operator (PISO) and the Semi-Implicit Method for Pressure-Linked Equations Revised (SIMPLER) algorithms. The FANS code has undergone rigorous validation and has been successfully employed in investigating complex flow problems in various research studies (Ye and Chen, 2019; Huang and Chen, 2021; Huang et al., 2022; Kim et al., 2022; Chen and Chen, 2023).

2.2. Quantification of numerical uncertainties in CFD predictions

To establish credibility from CFD predictions, the numerical errors and uncertainties in the CFD simulations need to be scrutinized. Although often mentioned together, the "errors" and "uncertainties" are conceptually different. In short, the term "errors" represents the discrepancy between numerical predictions and the "exact" solutions, whereas "uncertainty" encompasses a range within which the "exact" solution is expected to lie with a specified level of confidence (Roache, 2009). In CFD simulations, three main categories of numerical errors are commonly encountered: round-off errors, iterative errors, and discretization errors (Eça et al., 2019). Hence, the complete numerical error εn can be represented as:

$$\epsilon_n = \epsilon_{ro} + \epsilon_{it} + \epsilon_d \tag{12}$$

The round-off error ϵ_{ro} arises from the finite floating-point precision of computers. However, this term is treated small when modern computing machines are used, i.e. double-precision computers. The iterative error ϵ_{it} stems from the non-linearity nature of the partial equations. However, it can be minimized by imposing a strict convergence criterion during the solving process. Therefore, it is also considered to be insignificant. The discretization error ϵ_d, on the other hand, comes with the fact that algebraic equations are used to approximate the partial differential equations, and is thus believed to exert a predominant influence among the numerical errors in CFD simulations. Consequently, it constitutes the primary focus of the current work.

The method used to quantify the numerical uncertainty associated with the discretization error is referred to as the verification procedure. This procedure aims to estimate the discretization uncertainty U_d of a given result φ_i when the exact solution φ_0 is unknown (Make and Vaz, 2015). The verification procedure utilized in this study is based on the approach proposed by Eça and Hoekstra (2014). In the case of unsteady simulations, the discretization error can be represented as a power series as:

$$\epsilon_d \simeq \delta_d = \varphi_{ij} - \varphi_0 = \alpha_x h_i^{p_x} + \alpha_t t_j^{p_t} \tag{13}$$

In the aforementioned equation, φ_{ij} represents any quantity derived from a CFD simulation utilizing grid i and time increment j. The estimated "exact" solution, denoted by φ_0, is obtained by fitting a set of φ_{ij} (e.g., $\varphi_{11}, \varphi_{22}$, and φ_{32}) in a specific manner. The observed orders of convergence in space and time are represented by p_x and p_t, respectively. The relative grid and time step sizes are denoted by h_i and t_j, respectively. In the case of CFD simulations employing structured grids and fixed time step sizes, such as those utilized in the present study, h_i and t_j

are defined by the following equations:

$$h_i = \frac{\xi_{\text{cell } 1}}{\xi_{\text{cell } i}} \tag{14}$$

$$t_j = \frac{\Delta t_j}{\Delta t_1} \tag{15}$$

where $\xi_{\text{cell } i}$ denotes the number of cells in any of the three directions in grid i, and Δt_j denotes the time step size of the time increment j. It should be pointed out for structured grids, a same value of the relative grid size h_i is applied to each of the three directions, i.e. ξ, η, and ζ. In addition, the finest spatial or temporal resolution are labeled by a subscript of 1. Consequently, in the simulation that utilizes the finest grid spacing and time step size, both h_i and t_j are equal to 1.

It is worth noting that Equation (13) involves 5 unknowns, which means that a minimum of 5 simulations with varying pairs of h_i and t_j is required to determine these unknowns. However, it is advisable to conduct additional simulations in order to estimate the errors using following this approach as suggested by Eça and Hoekstra. The 5 unknowns, namely φ_0, α_x, p_x, α_t, and p_t, are determined by minimizing the following function in a least-square manner:

$$S_{RE}(\varphi_0, \alpha_x, p_x, \alpha_t, p_t) = \sqrt{\sum_{i=1}^{n_g} \sum_{j=1}^{n_t} w_{ij} \left[\varphi_{ij} - \left(\varphi_0 + \alpha_x h_i^{p_x} + \alpha_t t_j^{p_t} \right) \right]^2} \tag{16}$$

In the above expression, the total number of different computational grids and time increments used in the verification study are denoted by n_g and n_t, respectively. The weight assigned to a particular CFD prediction, w_{ij}, allows one to discriminate between the various pairs of h_i and t_j in terms of their relative accuracy. For example, predictions obtained from finer sets of h_i and t_j are given higher weights. The estimated exact solution φ_0 can thus be derived after the least-squares fitting, allowing for the estimation of the discretization errors and uncertainties of the CFD predictions. It should be noted here that comparing to the verification procedure proposed by Celic et al. (Celik et al., 2008). Which is commonly used in the identification of discretization errors in CFD simulations, the procedure adopted in the current work determines the parameters, i.e. φ_0, α_x, p_x, α_t, and p_t, through a least-square fitting instead of using a deterministic relation (Eça and Hoekstra, 2009), and it is found to be the most robust approach for its ability to cope with nonconforming observed-order-of-convergence and otherwise anomalous convergence behavior (Van Der Kolk et al., 2020). For more details of the procedure adopted in the current work and the comparisons of different verification approaches, please refer to Eça and Hoekstra, 2009, 2014, Burmester et al. (2020), and Van Der Kolk et al. (Van Der Kolk et al., 2020). Ideally, quantification of experimental uncertainties is also needed when comparing the numerical predictions to experimental measurements. However, this information is absent in the NTNU BT1 experiment as adopted in the current study. Therefore, we will directly compare the current CFD predictions including the uncertainty ranges against the experimental measurement.

3. Code verification: simulation of the S826 airfoil

The current study incorporates two experiments conducted at NTNU: a wind tunnel test for the S826 airfoil (Bartl et al., 2019) and the NTNU BT1 experiment (Krogstad and Eriksen, 2013). This section will provide a detailed description of these two experiments.

3.1. Test case description

The blades of the NTNU BT1 wind turbine were designed and manufactured by utilizing the (National Renewable Energy Laboratory) NREL S826 airfoil. Fig. 1 illustrates the shape of the NREL S826 airfoil.

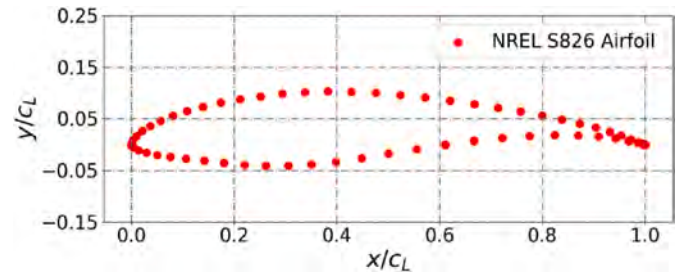Therefore, served as a benchmark, the performance of the NREL

Fig. 1. NREL S826 airfoil.

S826 airfoil (Bartl et al., 2019) is initially evaluated through CFD simulations. In this experiment, a wing section using the S826 airfoil is tested in the wind tunnel at NTNU. Surface pressure distribution of the wing section are recorded in the experiment under different inflow velocities and angles of attack (*AoA*).

The wing section used in the experiment has a chord length of $c_L = 0.45\ m$ and a total span length of $1.78\ m$. The pressure distribution on the central wing section is measured at four different *AoA*: $0°$, $4°$, $8°$, and $12°$. The authors argued that the errors in pressure measurement are within $\pm 0.03\%$. For each of the four *AoA* values, pressure measurements are taken under eight different inflow conditions. The inflow velocity ranges from 1.47 m/s to 22.27 m/s while the corresponding turbulence intensity level (*T I*) decreased from 0.71% to 0.26%. Consequently, the chord-based Reynolds numbers (*Re*) increased from 0.5×10^5 to 6.0×10^5. For more comprehensive information regarding this experiment, readers are encouraged to reference the original report (Bartl et al., 2019). The experimental setup of the wing section in the wind tunnel is illustrated in Fig. 2.

The local Re and *AoA* as a function of the rotor radius at *TSR* = 6 are shown in Fig. 3. Examination of the graph indicates that, at *TSR* = 6, the local Re for majority of the blade span locations is approximately 1.0×10^5, and the range of local *AoA* of the blade is roughly from $7°$ to $16°$. Consequently, in the context of the current benchmark case involving the S826 airfoil, CFD simulations will be carried out with Re set at 1.0×10^5 and *AoA* varying at $4°$, $8°$, and $12°$. The results obtained from the CFD simulations will be compared against the experimental measurements.

Fig. 2. Experimental configuration of the NREL S826 airfoil wing section test, adopted from (Bartl et al., 2019).
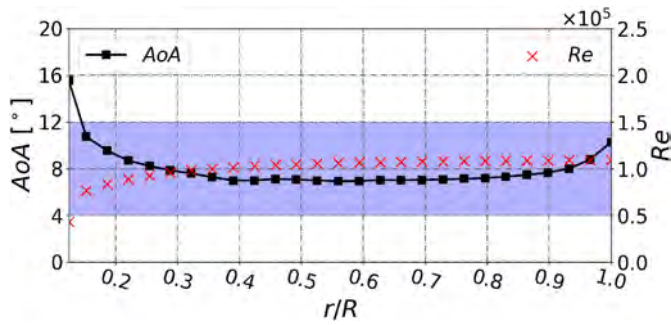
Fig. 3. Re and *AoA* along the wind turbine blades at the design *TSR* of 6.

3.2. Numerical setup

3.2.1. Computational domain and grid generation

The computational domain depicted in Fig. 4 has been tailored to correspond with the dimensions of the wind tunnel walls utilized in the experimental setup. Additionally, the figure illustrates the designated names for the boundaries within this domain. To define the coordinate system, the positive *x*-axis is oriented from the inlet to the outlet, the *y*-axis pans from bottom to top, and the *z*-axis is therefore defined according to the right-hand rule.

Next, structured overset grids are created within the computational domain. Fig. 5 provides an overview of the resulting computational grids, with distinct colors leveraged to differentiate between individual grid blocks. Furthermore, a detailed description of the grid generation process for this benchmark case is provided, and this illustration will be used as an example for the grid generation process in FANS simulations. The following steps are undertaken in this process.

- Three mutually overlapped structured overset grid blocks are generated, i.e. the boundary-layer block, the intermediate block, and the background block. Specifically, the thickness of the first-layer cells of the boundary-layer block satisfies the criterion of non-dimensional wall distance less than one, i.e. $y^+ < 1$. A normal extrusion method is used to ensure the quality of the computational cells within the boundary-layer blocks, and a cell expansion ratio of 1.2 is applied in the wall-normal direction.
- The total number of processors needed in the simulation is determined. For example, in this case, we use 28 processors in the simulations.
- The three aforementioned overset grid blocks are decomposed into 28 smaller blocks, ensuring that each processor can handle a distinct overset grid block. It is worth noting that the number of grid points in each small grid block must be similar to ensure that the processors complete their calculations within a similar duration during parallel computations.
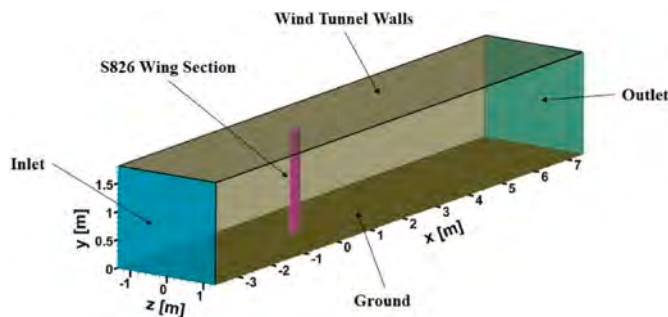
- Boundary conditions for the 28 blocks are individually prepared and distributed into the 28 processors for parallel computation.

Therefore, it can be observed from Fig. 5 that the original background block has undergone a re-blocking process, resulting in 6 smaller blocks. Similarly, the original intermediate block has been re-blocked into 15 blocks, while the original boundary-layer block has been re-blocked into 7 blocks. It is worth mentioning that one can conveniently obtain the corresponding computational grids at different AoA by simply rotating the boundary-layer blocks, so that only one computational grid needs to be constructed. This approach offers superior efficiency and time-saving advantages compared to simulations utilizing fully-connected grids, which necessitate separate generation of computational grids for each distinct *AoA*. For a single case, the total number of grid points approximates 2 million.

Fig. 6a shows the cross-sectional views of the overset grids. It can be seen that different grid blocks are overlapped. In the interpolation regions of two overlapping blocks, a grid point of a certain block receives information from the surrounding points of another block through interpolation. Those grid points receiving data are called receiver grids and those which provide information for interpolation are called donor grids. An illustration of the donor and receiver grids is provided in Fig. 6b.

It is important to reiterate that the primary objective of the present benchmark study is to showcase the capacity of FANS in simulating the S826 airfoil. Consequently, the CFD predictions will be directly compared to the measured data, and therefore, the verification study aimed at quantifying the numerical uncertainties associated with spatial or temporal discretization errors will not be included in this analysis.

3.2.2. Numerical settings

For the inlet and the outlet boundaries, a constant inflow and a linear-extrapolation condition is specified, respectively. The wing section's surface is treated as a non-slip wall, whereas the wind tunnel walls are treated as slip-walls for numerical robustness and computational efficiency. Although not presented here, simulations with non-slip tunnel walls were also conducted, no obvious discrepancies were found in those results. Interpolation will be carried out using the flow data from the donor grids. This is accomplished by designating the boundary conditions of those surfaces that intersect with other blocks as "interior boundary surfaces". The chord length is utilized to derive the value of Re used in this study, which is roughly 1.0×10^5,

3.3. Simulation results

The benchmark simulations utilized the Intel Xeon 6248R (Cascade Lake) processors, running at a clock speed of 3.0 GHz with 24 cores. Each simulation requested the allocation of 28 cores and was successfully completed within a timeframe of 4 h.

The figure depicted in Fig. 7 illustrates the normalized velocity magnitude contours (defined by *UMag/Uref*) and the normalized pressure contours (defined by Eq. (17)) for the wing section at the mid-span. It is evident that as *AoA* increases, there is a corresponding reduction in pressure on the suction side of the airfoil, signifying an augmentation in lift generation. Furthermore, within the velocity contours, the airflow exhibits sustained attachment to the surface at an *AoA* of 4°, while initiating separation from the surface at higher *AoA* values.

Fig. 8 presents the comparison between the CFD-predicted surface pressure and the measured data at the mid-span of the wing section. To differentiate the results obtained from the five distinct overset-grid blocks, namely Sec01 to Sec05, varying colors are employed. Additionally, the pressure coefficient (C_{pn}), which quantifies the pressure relative to the freestream conditions, is defined by the following equation:

Fig. 4. Illustration of the computational domain for the S826 airfoil calculations.
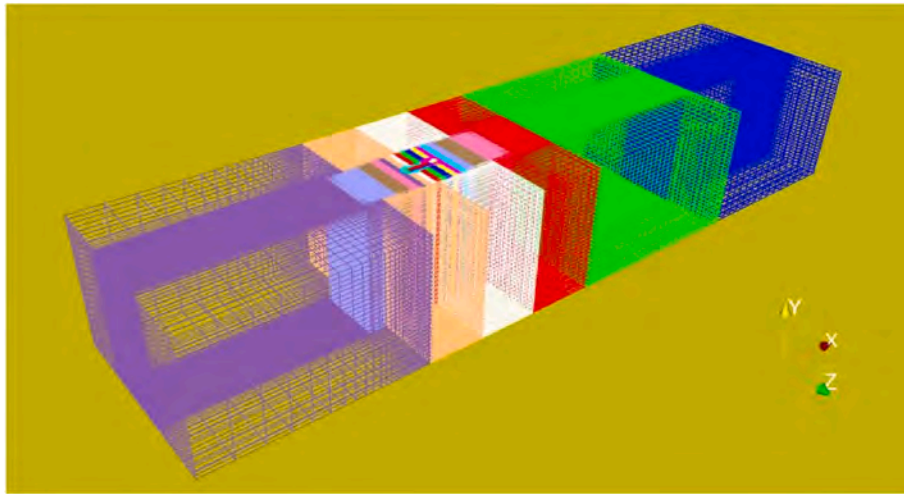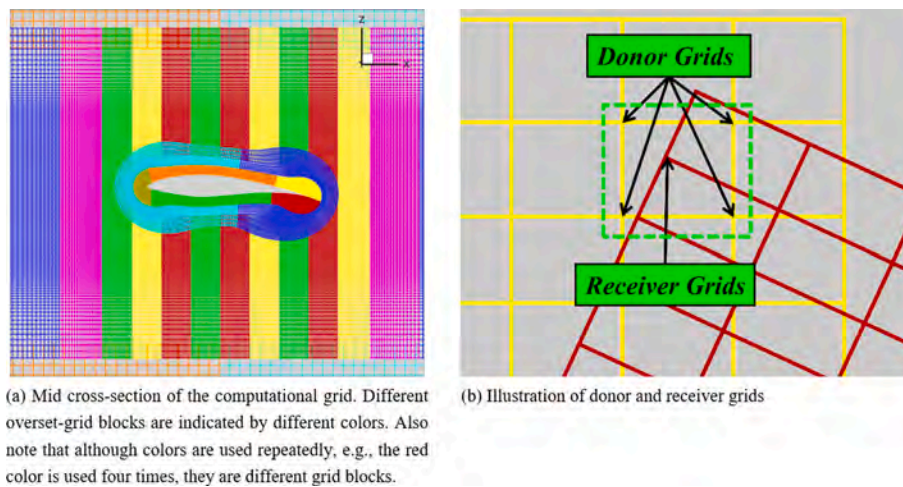
Fig. 5. Overset grid for the simulations of the S826 airfoil wing section. Different colors are utilized to differentiate between the grid blocks.

(a) Mid cross-section of the computational grid. Different overset-grid blocks are indicated by different colors. Also note that although colors are used repeatedly, e.g., the red color is used four times, they are different grid blocks.

(b) Illustration of donor and receiver grids

Fig. 6. Mid cross-section of the computational grid used in the simulations and the illustration of donor and receiver grids.

$$C_{pn} = \frac{p}{\frac{1}{2}\rho U^2} \quad (17)$$

In general, good agreement between the predicted surface pressure of the S826 airfoil wing section and the measured data at the mid-span is achieved, demonstrating the ability of the FANS code in the accurate predictions of the surface pressure of the S826 airfoil at the Re around 1.0×10^5.

4. Quantification of numerical uncertainties in the CFD-predicted wind turbine performance: verification

In this section, we perform a systematic verification study to quantify the discretization uncertainties of the CFD-predicted wind turbine performance. First, the definition of the computational domain, the grid generation strategies, and the numerical settings, are introduced. Then, the verification procedure adopted in the present study is applied to assess the discretization uncertainties of the CFD-predicted turbine performance. The numerical uncertainty determined from the verification study at $TSR = 6$ will then be extended to cover the entire range of TSR values, and comparisons will be made with other representative numerical results and against the experimental data.

4.1. Test case description

In 2008, NTNU initiated a series of wind tunnel experiments featuring diverse configurations and inflow conditions. Prior to the release of the experimental data, blind comparison workshops were convened to assess the performance of computational models when provided solely with the turbine geometry (Krogstad and Eriksen, 2013). This distinctive attribute sets the NTNU blind test series apart from other wind tunnel examinations, as it encompasses experiments for both single and dual wind turbines, rendering it a highly suitable benchmark for numerical simulations targeting wind turbine aerodynamics. In BT1, a horizontal-axis wind turbine with three blades was tested in a closed-loop wind tunnel. Each of the blades was designed by using the NREL S826 airfoil. The dimensions of the wind tunnel itself are specified as 11.15 *m* in length and 2.71 *m* in width. Notably, the inlet height measures 1.801 *m*, while the outlet height registers at 1.851 *m*. The rotor, characterized by a diameter of 0.894 *m* (referred to as D), is centrally located along the tunnel's axis, positioned at a distance of 3.66 *m* from the inlet, and elevated 0.817 *m* above the floor level. To facilitate further analysis, the organizer has made the CAD file associated with the rotor configuration openly accessible. For a visual representation of the experimental arrangement, refer to Fig. (9).

In the experiment, a constant inflow velocity of 10 m/s and turbulence intensity level (*TI*) of 0.3% were specified for all test cases. As
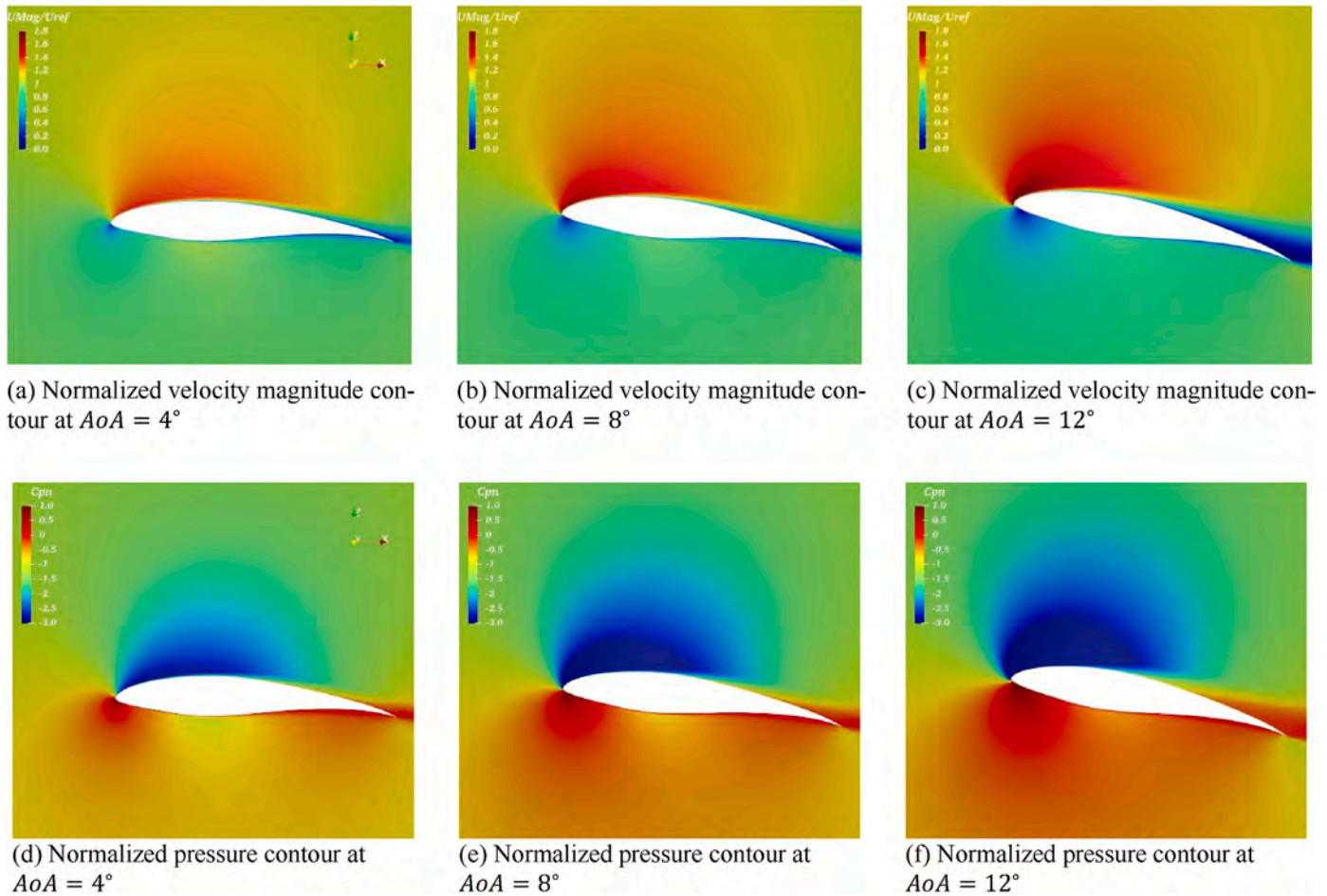
(a) Normalized velocity magnitude contour at $AoA = 4°$

(b) Normalized velocity magnitude contour at $AoA = 8°$

(c) Normalized velocity magnitude contour at $AoA = 12°$

(d) Normalized pressure contour at $AoA = 4°$

(e) Normalized pressure contour at $AoA = 8°$

(f) Normalized pressure contour at $AoA = 12°$

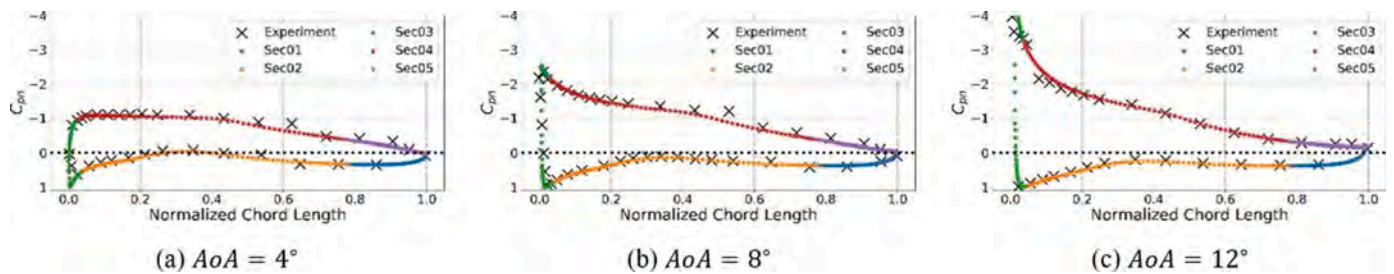**Fig. 7.** Contours of the normalized velocity magnitude (*UMag/Uref*) and the normalized pressure (Eq. (17)) at Re of 1.0×10^5.

(a) $AoA = 4°$

(b) $AoA = 8°$

(c) $AoA = 12°$

Fig. 8. Surface pressure at the mid-span of the S826 airfoil wing section for Re of 1.0×10^5. Different colors are utilized to differentiate the different overset-grid blocks covering the surface of the wing section.

indicated by Krogstad et al., the inlet flow remains uniform within $\pm$ 0.5% over the rotor's swept area. Varying values of *TSR* were attained by adjusting the wind turbine's rotational speed. The performance characteristics, namely the thrust coefficient C_T and the power coefficient C_P, as well as the mean wake profiles, of the wind turbine was recorded in the measurement. For more information on the NTNU BT1 experiment, the readers are encouraged to reference the original reports (Krogstad et al., 2011; Krogstad and Eriksen, 2013). For further details on the NTNU BT1 experiment, readers are encouraged to consult the original reports (Krogstad et al., 2011; Krogstad and Eriksen, 2013). The current study concentrates on quantifying the numerical uncertainties in CFD predictions of turbine performance. Although the same process can be used for analyzing wake characteristics, it necessitates distinct grid refinement and simulation strategies, and thus will not be presented in this work.

It is worth mentioning that the forthcoming verification study, which aims to evaluate numerical uncertainties of the CFD-predicted wind turbine's performance, will be carried out at the designed *TSR* of 6. Upon obtaining the numerical uncertainty at this specific *TSR*, it will be propagated to the results attained at other *TSR* values. While it is technically ideal to assess uncertainties for each *TSR* value separately, this approach involves conducting at least six additional simulations for each *TSR* value, rendering it impractical for engineering applications due to limited computational resources. Hence, in this study, the design *TSR*, typically chosen as a representative operating condition, has been selected as the basis for the analysis (Make and Vaz, 2015; Xie and Archer, 2017), with *TSR* set at 6.

Furthermore, the equations defining C_T, C_P and *TSR*, as introduced earlier, are as follows:
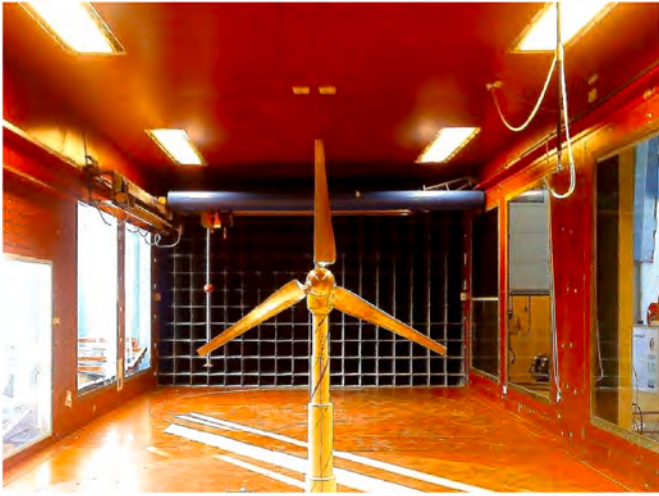
Fig. 9. Experimental setup of the BT1 wind turbine test, adopted from (Krogstad and Eriksen, 2013).

$$C_T = \frac{T}{\frac{1}{2}U_{ref}^2 A} \tag{18}$$

$$C_P = \frac{Q\Omega}{\frac{1}{2}U_{ref}^3 A} \tag{19}$$

$$TSR = \frac{R\Omega}{U_{ref}} \tag{20}$$

In the above expressions, R refers to the rotor diameter, A represents the area of the rotor plane, U_{ref} is the free-stream velocity, and Ω is the rotor's angular velocity. Furthermore, T is the thrust of the turbine while Q being the torque.

4.2. Numerical setup

The calculations in this verification study are executed by Intel Xeon E5-2680 processors. Each of the simulations is run in parallel on 52 processors and requires a wall time of approximately 1–3 days, depending on the computational grid and time configuration. The simulations are run for 7 turbine revolutions within which the output of the turbine performance has reached a steady-state region.

4.2.1. Computational domain and grid generation

First, the computational domain is defined for the simulations. The computational domain's outer boundaries align with the wind tunnel walls in the experim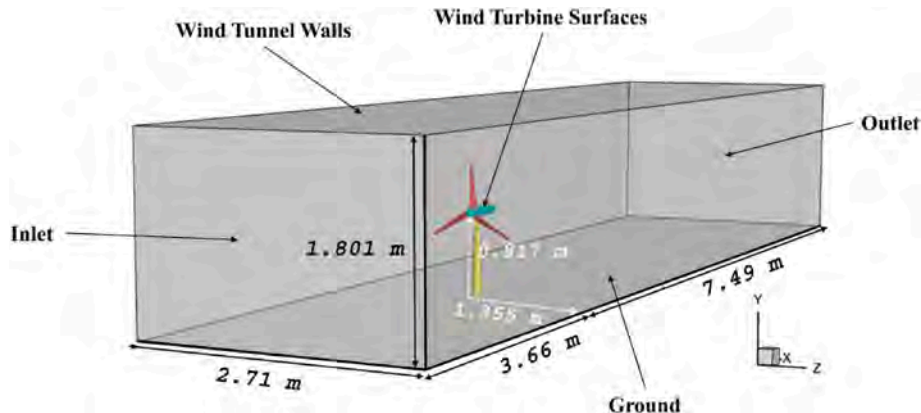ental setup. Fig. 10 provides an illustration of the computational domain. The coordinate system is defined as follows: the origin is located at the rotor center, and the orientations of the three axes are the same as those in the benchmark simulations of S826 airfoil section as described in Sec. 3.

Afterward, as shown in Fig. 11, the entire domain is partitioned roughly into two parts, i.e. the inner rotating part (yellow) which encompasses the rotor (red) and the outer stationary part (white). By doing this, we can conveniently change the grid resolutions of the overset grid blocks in each of the two separate parts, while keeping the other untouched. This approach is particularly advantageous in the present investigation since only the grid resolution near the rotor surfaces significantly impacts the predictions of C_T and C_P, while the influence of spatial resolution in the wake on the wind turbine's performance characteristics is negligible (Ye et al., 2022, 2023a; Xie and Archer, 2017). Consequently, substantial computational resources can be conserved by reducing the grid resolution of the overset-grid blocks in the stationary outer region. It should be noted that the whole disc as shown in yellow in Fig. 11 is rotating with the rotor in the current work. By rotating the whole disc instead of only the hub and blades, more robust interpolation and better solution of the fluid field can be achieved in the simulations. Otherwise, a much finer temporal spacing maybe required to avoid orphan points, i.e. points that cannot find any interpolation, in the CFD simulations with overset grids.

Overset-grid blocks with structured computational grids are then generated. Because in the current study, the target is the performance characteristics of the turbine, different computational grids in the inner rotating part are generated while they all share a same grid resolution in the outer stationary part. These grids, labeled as G1 to G3, range from the finest grid representation (G1) to the coarsest grid representation
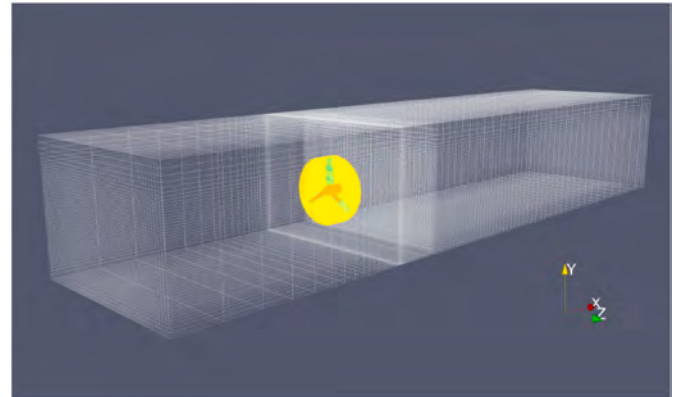

Fig. 11. Illustration of the overset grid blocks of the inner rotating and the outer stationary parts.

Fig. 10. Computational domain used in the CFD simulations of the NTNU BT1 wind turbine.

(G3). Each of the three grids comprises a total of 93 grid blocks, inclusive of three phantom grid blocks utilized for hole-cutting purposes. Fig. 12a and b shows an overview and the surface blocks of the generated grids.

Boundary layer blocks are created on the surfaces of the wind turbine, encompassing the blades, hub, nacelle, and tower. These blocks adhere to the criterion of $y^+ \leq 1$ while maintaining a cell expansion ratio normal to the wall of 1.2. Furthermore, Table 1 provides a summary of the number of grid points in each direction within the boundary layer blocks of the three grids. It is important to note that in CFD simulations utilizing overset grids, the grid cell sizes of different blocks within the overset regions should be approximately equal. This is crucial to facilitate a seamless interpolation of flow variables among neighboring blocks. Therefore, as shown in Fig. 13a, intermediate blocks (cyan) are designed to close the size difference between the boundary layer blocks (red) and the background disc blocks (yellow). Cross-sectional views are also provided to show the details of the overset-grid structure in the vicinity of the blade surfaces, as shown in Fig. 13b.

4.2.2. Numerical settings

Same as the settings in the S826 airfoil simulations, for the inlet and the outlet boundaries, a constant inflow and a linear-extrapolation condition is specified, respectively. The surfaces of the wind turbine are treated as no-slip walls, whereas the wind tunnel walls are treated as slip-walls for numerical robustness and computational efficiency. Although not presented here, simulations with non-slip tunnel walls were also conducted, no obvious discrepancies were found in those results. Interpolation will be carried out using the flow data from the donor grids. This is accomplished by designating the boundary conditions of those surfaces that intersect with other blocks as "interior boundary surfaces". A two-layer $k - \epsilon$ model is adopted for turbulence closure, as already detailed in Section 2.1.2. The value of Re utilized in this study is computed at the blade tip, resulting in a chord-based Re of 1.036×10^5.

4.3. Verification study at the design TSR

In this particular verification study, an analysis is conducted to assess the uncertainties arising from both spatial and temporal discretizations. To achieve this, a simulation matrix is constructed by employing three systematically refined computational grids in combination with three distinct time increments. The three computational grids utilized in this study are summarized in Table 2. The relative grid size, denoted as h_i, is computed using Equation (14). Meanwhile, the number of grid points within the refined blocks is indicated as N_R^i, and the total number of grid points in each computational grid is denoted by N_T^i. It is crucial to

Table 1

Number of grid points specified in each direction of the blade boundary layer blocks of the BT1 wind turbine.

| Grids	Circumferential	Wall-Normal	Spanwise
G1	176	48	203
G2	147	40	169
G3	123	33	141

emphasize that, for the purpose of this verification study, only the overset blocks located within the inner rotating part are subjected to refinement. In contrast, the grid blocks in the outer stationary part remain unchanged throughout all calculations. As a result, the computation of h_i exclusively considers the inner rotating part when determining grid size variations.

Table 3 provides a comprehensive overview of the three different time increments used in the computations. The smallest and largest time increments are labeled as T1 and T3, respectively. The relative time increment, t_j, is determined using Equation (15), while the actual time increment is denoted by Δt_j. The final column lists the number of time steps required for the wind turbine to complete one full rotation. It is noteworthy that a value of $t_j = 1.5$ corresponds to a rotational angle of $3.0°$ per time step in the simulations. In order to ensure that a "periodic stage" is reached, 7 turbine revolutions were simulated in each simulation. Afterward, the values of C_T and C_P were calculated by averaging the results obtained during the last two revolutions.

It is important to note that in Equation (13) and Equation (16), there are only 5 unknowns, and therefore, theoretically, 5 datasets obtained from 5 simulations should be adequate. However, based on the recommendation in (Eça and Hoekstra, 2014), an additional dataset is preferred in the verification process when fitting the data points using a least-squares approach. In line with this guidance, CFD simulations will be conducted for 6 combinations of h_i and t_j in the present study. A summary of the selected combinations of h_i and t_j is outlined in Table 4.

4.3.1. Iterative convergence

To solve the incompressible Navier-Stokes equations, two types of iterations are generally utilized: the inner loops and the outer loops. After the original partial differential equations have been discretized into algebraic equations, they are typically solved in an iterative manner. These iterations used to solve the algebraic equations are usually referred to as inner loops. Typically, thanks to the effective matrix solvers, a large number (e.g., several hundred) of iterations is set and a low convergence level is specified for the inner loops, resulting in negligible iterative errors regarding solving the individual equations. On
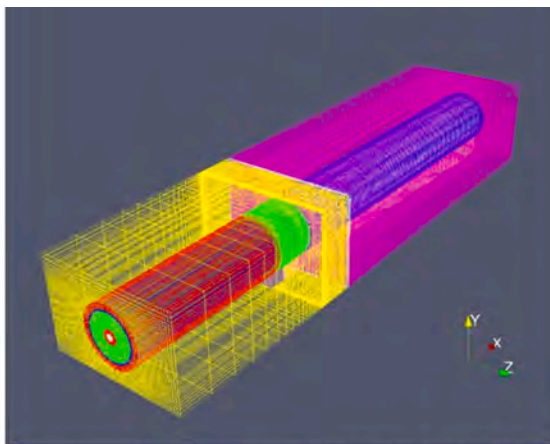
(a) Overview of the overset grid blocks used in the simulations.
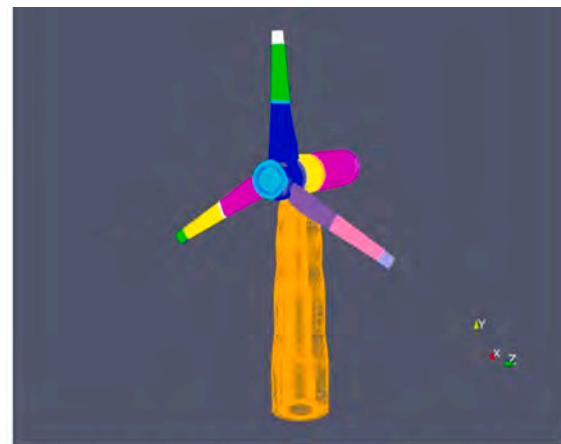
(b) Overset-grid blocks covering the surfaces of the wind turbine.

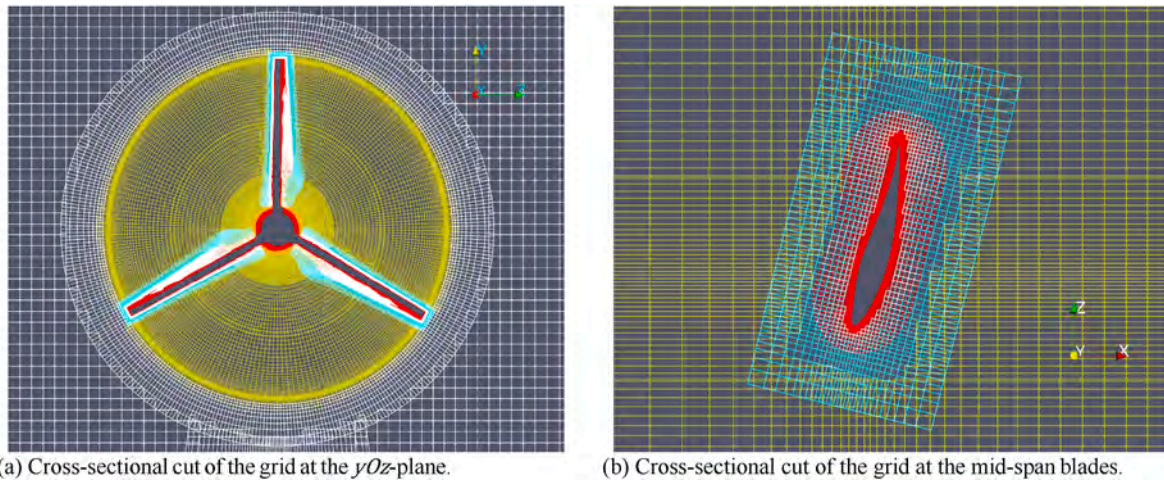**Fig. 12.** Configuration of the overset-grid blocks.

(a) Cross-sectional cut of the grid at the *yOz*-plane.

(b) Cross-sectional cut of the grid at the mid-span blades.

Fig. 13. Cross-sectional cuts of the computational grids.

Table 2
Information of the computational grids.

Grids	h_i	N_R^i [million]	N_T^i [million]
G1	1.00	10.47	14.78
G2	1.20	6.03	10.22
G3	1.44	3.48	7.58

Table 3
Information of the computational grids.

Time increments	t_j	Δt_j [s]	No. Time steps per revolution
T1	1.0	0.00026	180
T2	1.5	0.00039	120
T3	2.0	0.00052	90

Table 4
Selected configurations adopted in the verification study.

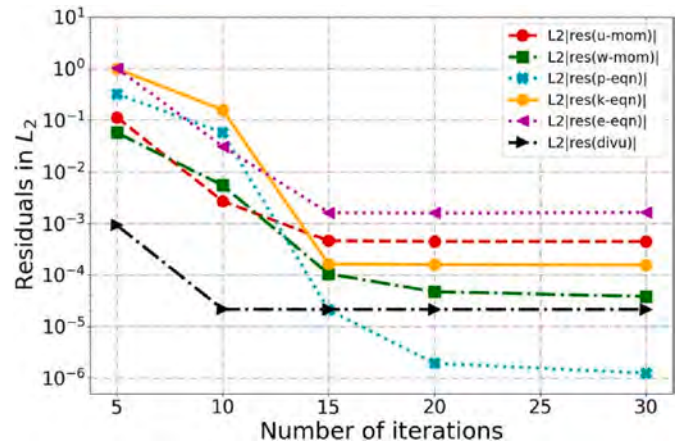|	T1	T2	T3
G1		✓	
G2	✓	✓	✓
G3	✓		✓

Fig. 14. Change of L_2-norm of the residuals with the increase of outer iterations.
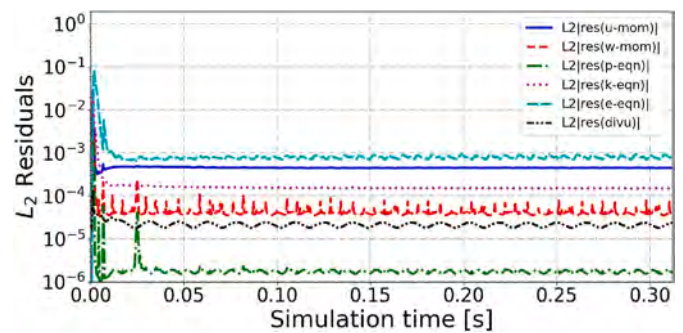
Fig. 15. Histories of L_2-norm of the residuals in FANS simulations.

the other hand, the outer loop is utilized to achieve velocity-pressure coupling to ensure the maintenance of fluid incompressibility. In contrast to the inner loops, relatively fewer iterations are usually employed for the outer loop in CFD simulations. Specifically, according to our experience, the results obtained by using the FANS code can be sensitive to the number of iterations used in the outer loop. Therefore, to determine the optimal number of iterations for the outer loop, a preliminary test is conducted. The results of this test are presented in Fig. 14, where the L_2-norm of the residuals in the simulations is plotted against the number of iterations used in the outer loop. The figure demonstrates that although the residual levels decrease as the number of iterations increases, there is no significant reduction beyond 20 iterations. Therefore, 20 iterations for the outer loop will be adopted in the following simulations.

The iterative convergence of case G2T2 is depicted in Fig. 15 through the representation of residual levels. It is evident that the L_2-norm of the residuals for all variables has reached or fallen below the threshold of 10^{-3}, and has demonstrated stability throughout the simulations. This observation indicates that the simulation has achieved satisfactory convergence, with the iterative errors ϵ_{it} as defined in Eq. (12) being

sufficiently small to be justifiably neglected in the estimation of numerical uncertainties.

Fig. 16 presents the surface pressure distribution on the wind turbine along with the corresponding velocity field on the rotor plane, specifically the *yOz*-plane, at various rotation angles. It is important to note that the rotation angle refers to the angle between the tower and the blade when it is vertically oriented downwards, as illustrated in Fig. 16c. Upon observing the figure, it is evident that the velocity field obtained is continuous and smooth, confirming the convergence of the simulation. Additionally, it demonstrates that the interpolation of flow information
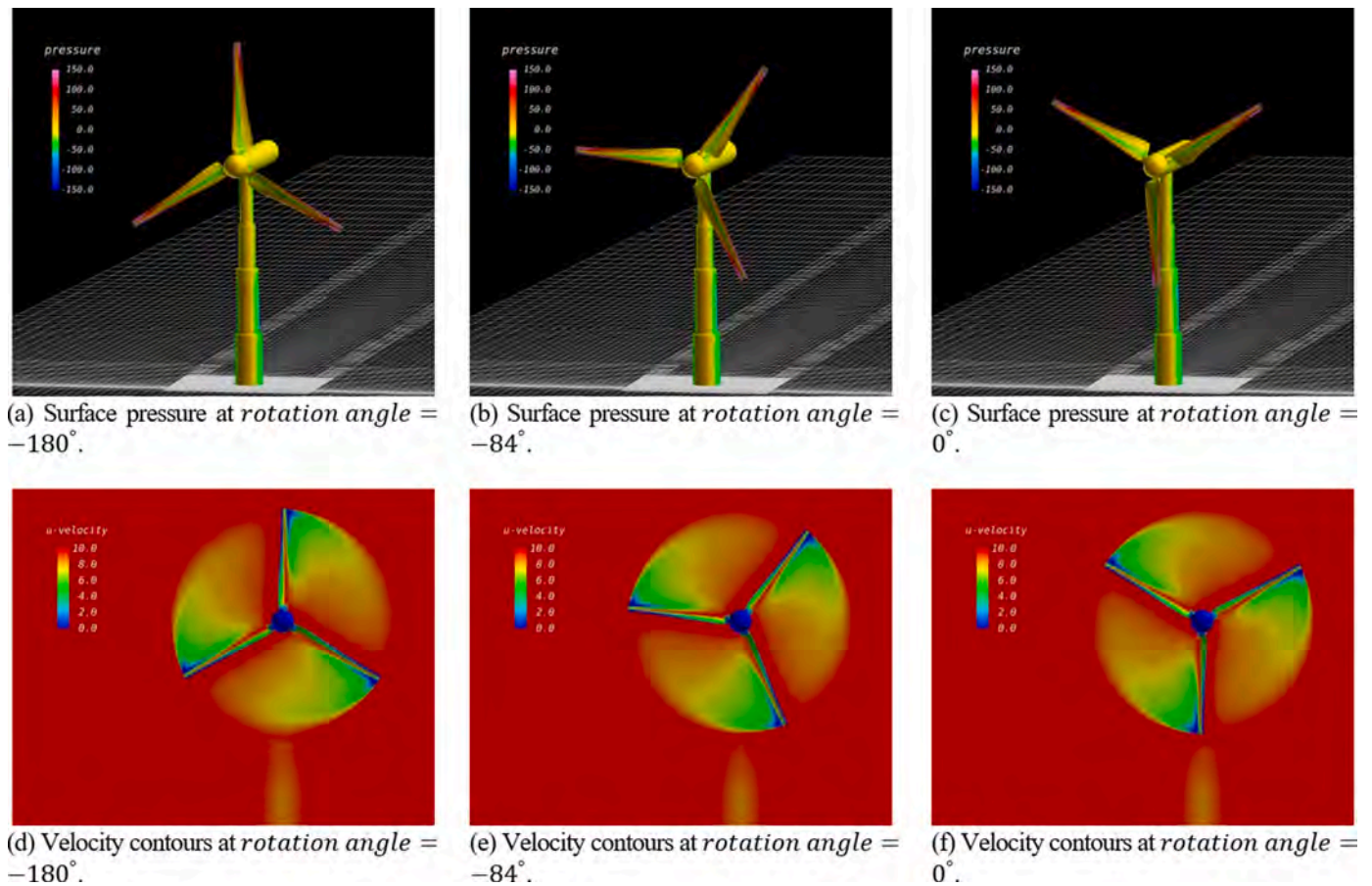
(a) Surface pressure at *rotation angle* = −180°.

(b) Surface pressure at *rotation angle* = −84°.

(c) Surface pressure at *rotation angle* = 0°.

(d) Velocity contours at *rotation angle* = −180°.

(e) Velocity contours at *rotation angle* = −84°.

(f) Velocity contours at *rotation angle* = 0°.

Fig. 16. Contours of surface pressure and the corresponding rotor-plane velocity for the NTNU BT1 wind turbine at various rotation angles.

among different overset grid blocks by FANS has been accurately performed.

4.3.2. Discretization uncertainty

Figs. 17 and 18 present the predicted values of C_T and C_P, respectively, obtained from the six simulation cases. To enhance clarity, the results are organized in two ways: firstly, the results are grouped by relative time increments and plotted against relative grid size, as depicted in Fig. 17a and 18a; secondly, the results are grouped by relative grid sizes and plotted against relative time increment, as illustrated in Fig. 17b and 18b.

The variation in the thrust coefficient C_T can be observed in response to grid refinement, as depicted in Fig. 17a. It is evident that C_T decreases as the grid is refined from G3 to G1. Similarly, Fig. 17a also demonstrates that C_T decreases with the refinement of temporal spacing from T3 to T1. On the other hand, the power coefficient C_P exhibits a contrasting behavior. Fig. 18a illustrates that C_P tends to increase with grid refinement from G3 to G1. In addition, Fig. 18b shows that C_P decreases as the temporal spacing is refined from T3 to T1. These trends indicate that finer grids and coarser temporal spacing generally result in lower thrust and higher power coefficients.

In general, the quantities of interest, i.e. C_T and C_P, obtained from different combinations of grids and time step sizes are of similar magnitude and exhibit a monotonically increasing or decreasing trend
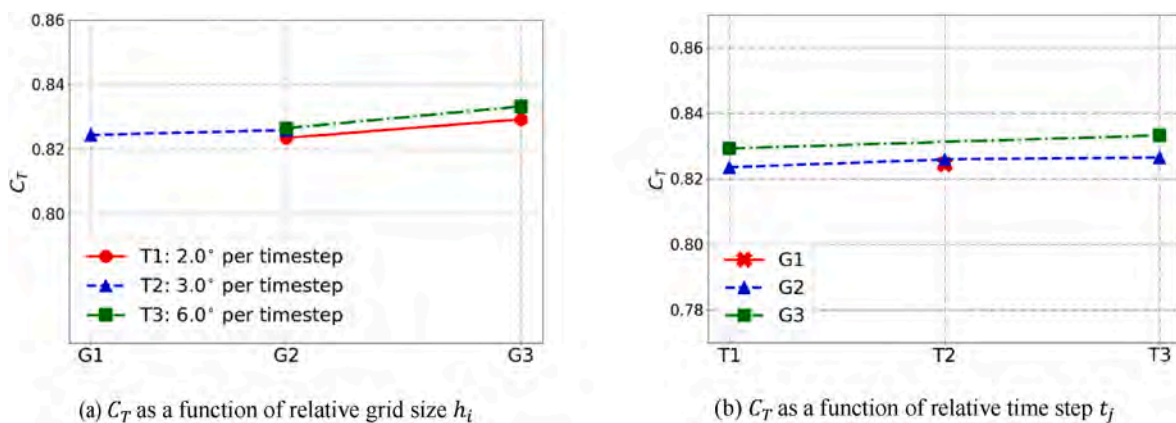

(a) C_T as a function of relative grid size h_i

(b) C_T as a function of relative time step t_j

Fig. 17. CFD predictions of C_T obtained from the simulation matrix. Note that the tick marks on the *x*-axis are positioned according to h_i or t_j as listed in Tables 2 and 3
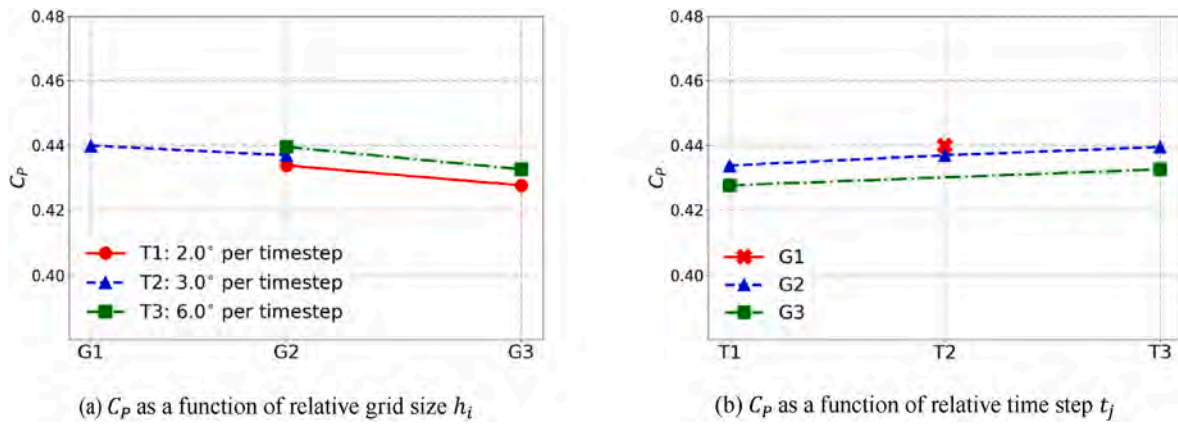
(a) C_P as a function of relative grid size h_i

(b) C_P as a function of relative time step t_j

Fig. 18. CFD predictions of C_P obtained from the simulation matrix. Note that the tick marks on the *x*-axis are positioned according to h_i or t_j as listed in Tables 2 and 3

when subjected to computational grid or time spacing refinement. This observation is, however, different from what the authors have found in a previous work (Ye et al., 2023a) in which an abnormal change of C_P was identified when the coarsest grid was used in the simulations. In that work, the same NTNU BT1 wind turbine was analyzed but a different CFD code, ReFRESCO, with unstructured computational grids were used. And the authors concluded that the sudden change of C_P is due to the insufficient resolution of the geometry at the blade tips, because the adopted unstructured grid generation method was not able to accurately attach the grid points to the body surface if the number of cells was too low. To the contrast, the body-fitted structured grid adopted in the current work can precisely reproduce the geometry of the blade geometries including the tip by using a relatively fewer number of grid points. More specifically, the total number of cells resolving the geometry of the blade tip, i.e. the leading edge, trailing edge, pressure side, and suction side, is more than 300 when C_P was observed to change abnormally as reported in that work (Ye et al., 2023a). As a comparison, for the G3, i.e. the coarsest grid in the current study, the number of points in the circumferential direction of the boundary layers blocks is only 123, as shown previously in Table 1.

Here, to strike a balance between accuracy and resources, the configuration of G2T2 are adopted for the subsequent CFD simulations to be performed at different *TSRs*. As a result, only the uncertainties associated with this specific case will be presented in the verification study.

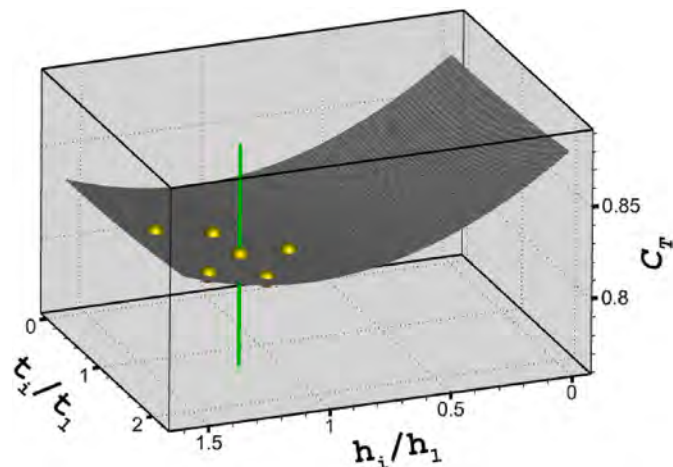Then, the verification procedure adopted in this study is applied to

the predicted values of C_T. As shown in Fig. 19, a curved surface is generated as a result of the least-squares fitting of the 6 data points. Note that the value of the curved surface at $(t_i/t_1, h_i/h_1) = (0, 0)$ is the extrapolated value of φ_0, which represents the theoretical value of C_T if an infinitesimal spacial and temporal size were used in the CFD simulations. The green vertical line represents the estimated discretization uncertainty of the corresponding numerical prediction, i.e. G2T2. The result of the fitting procedure is summarized in Table 5. The final error and the discretization uncertainty of the result obtained by case G2T2 are 5.4% and 7.3%, respectively.

Afterward, the same verification procedure is applied to the predicted values of C_P, as shown in Fig. 20. Again, a curved surface is generated as a result of the least-squares fitting of the 6 data points. The green vertical line represents the estimated discretization uncertainty of the corresponding numerical prediction, i.e. G2T2. A summary of the verification study is provided in Table 6. Consequently, the discretization error and uncertainty of C_P obtained from the configuration of G2T2 are 6.8% and 8.1%, respectively.

Hence, the discretization uncertainty of C_T and C_P calculated by using the configuration of G2T2 is estimated based on the 6 cases, which is 7.3% and 8.1%, respectively. Furthermore, it is worth noting that since the iterative uncertainties in the simulations were found to be negligible in earlier discussions, the total numerical uncertainty is assumed to be solely contributed by the discretization uncertainty. These obtained uncertainty ranges play a crucial role in the comparisons conducted afterward, as they provide a measure of the accuracy and reliability of the simulation results. It is essential to quantify the uncertainty in numerical simulations to ensure that the predictions are trustworthy and can be used confidently in practical applications.

4.4. Comparison with the experimental data

As mentioned earlier, the configuration of G2T2 is adopted in the subsequent CFD simulations. CFD calculations are then performed for *TSR* values of 2, 4, 8, 10, and 12. The CFD-predicted C_T and C_P are obtained and combined with the numerical uncertainties established in the verification study to compare against the experimental data.

The curves for C_T and C_P, obtained from the study, are depicted in

Fig. 19. Estimates of discretization uncertainty U_φ for the thrust coefficient C_T in case G2T2. The green line indicates the level of discretization uncertainty.

Table 5

Estimates of discretization error and uncertainty for the thrust coefficient C_T obtained using G2T2. The errors are expressed as a percentage of the extrapolated value φ_0.

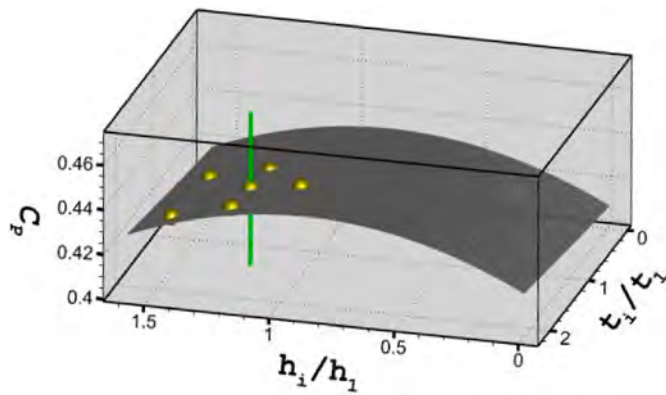| Quantity	Extrapolated value, φ_0	Solution of G2T2, φ_{22}	Error, ϵ_φ [%]	Uncertainty, U_φ [%]
C_T	0.873	0.826	5.4	7.3

Fig. 20. Estimates of discretization uncertainty U_φ for the thrust coefficient C_P in case G2T2. The green line indicates the level of discretization uncertainty.
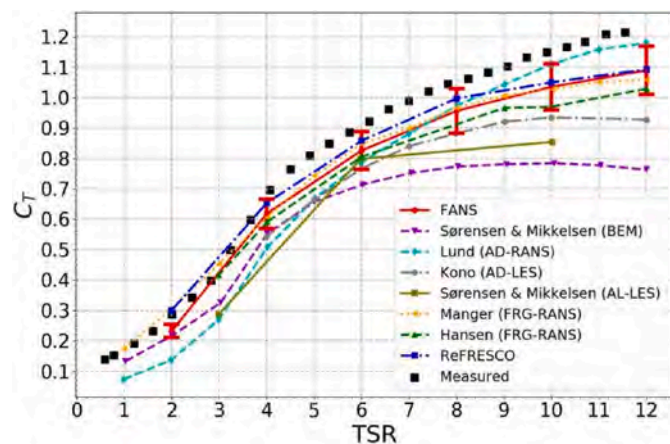
Table 6

Estimates of discretization error and uncertainty for the power coefficient C_P obtained using G2T2. The errors are expressed as a percentage of the extrapolated value φ_0.

| Quantity	Extrapolated value, φ_0	Solution of G2T2, φ_{22}	Error, ϵ_φ [%]	Uncertainty, U_φ [%]
C_P	0.409	0.437	6.8	8.1

Table 7

Information of the selected representative methods. BEM - blade element method; AD - actuator disc; AL - actuator line; FRG - fully resolved geometry.

Numerical Results	Rotor	Tower	Gov. Eq.	Turb. Closure	CFD Solver
Sørensen & Mikkelsen (BEM)	BEM	No	–	–	–
Lund (AD-RANS)	AD	No	RANS	$k - \omega$ SST	OpenFOAM
Kono (AD-LES)	AD	No	LES	Sub-grid	Front Flow/ red
Sørensen & Mikkelsen (AL-LES)	AL	No	LES	Sub-grid	EllipSys3D
Manger (FRG-RANS)	FRG	Yes	RANS	$k - \omega$ SST	Ansys Fluent
Hansen (FRG-RANS)	FRG	No	RANS	$k - \omega$ SST	STAR CCM+
ReFRESCO	FRG	Yes	RANS	$k - \omega$ SST	ReFRESCO
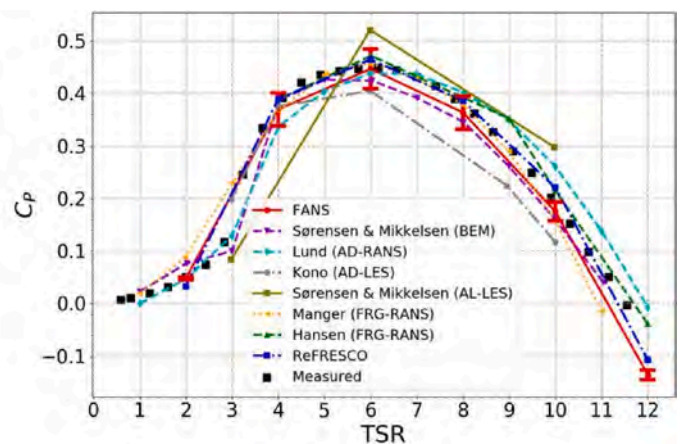
Fig. 21a and b respectively. Additionally, to facilitate comparison, the figures include results from other selected representative methods as reported in (Krogstad and Eriksen, 2013) and (Ye et al., 2023a). Detailed information regarding the selected numerical methods is presented in Table 7.

The CFD prediction of C_T in the current study obtained by using the FANS code aligns with the experimental data in overall trend. Notably, the experimental measurements fall within the uncertainty range until the *TSR* value reaches 8. However, for larger *TSRs*, denoted as the runaway state (Krogstad and Eriksen, 2013), the CFD-predicted values of C_T notably deviate lower than the measured data. This is, nevertheless, consistent with the results obtained by the other selected numerical methods.

Fig. 21a illustrates that, with the exception of Lund (AD-RANS), all methods exhibit a similar trend in predicting the C_T curve consistently under-predict the C_T values in the high *TSR* region. The numerical prediction labeled as Lund (AD-RANS), however, showcases the highest value of C_T for *TSR* greater than 8, while notably underestimates C_T for *TSR* lower than 4. Upon closer scrutiny, the values of C_T obtained by using the FRG-RANS framework generally surpass those obtained through BEM-based methods, such as AD and AL, particularly in the high *TSR* range. For the power coefficient C_P, as shown in Fig. 21b, the predicted values of C_P obtained in the current work are in good agreement with the measured C_P over the entire *TSR* range. It is noteworthy that all measured values of C_P remain within the uncertainty range.

The variance between the experimental measurements and the CFD-predicted C_T in the high *TSR* range could be attributed to the following factors:

- Unknown experimental uncertainty. Ideally, both numerical predictions and experimental measurements should be accompanied by comprehensive uncertainty reports, allowing for a robust comparison between the two. However, it should be noted that this aspect of the experiment was not explicitly documented in the original report (Krogstad and Eriksen, 2013). Specifically, the details of the experiment, such as whether it was replicated and the uncertainty of force measurement, were not reported. Consequently, the range of uncertainties associated with the experimental measurements of C_T and C_P are unknown. As a result, the contribution of experimental uncertainties to the current discussions has not been taken into account. This assumption may not be correct and could potentially be a factor contributing to the deviation observed between the numerical predictions and experimental measurements in the high *TSR* range.
- The observed discrepancy between experimental measurements and CFD-predicted C_T values in the high *TSR* range may be attributed to

(a) C_T curves.

(b) C_P curves.

Fig. 21. C_T and C_P at different *TSRs*. Basic information of the selected numerical methods are listed in Table 7.

various factors, one of which is blade pitch misalignment. Krogstad and Lund (Kim et al., 2022) have discussed this issue, highlighting that precise blade pitch adjustment is challenging due to the small physical size and complex blade geometry of the model wind turbine. Despite the development of a specialized alignment rig, an inherent uncertainty of 0.25° in the pitch angle persisted (Krogstad and Lund, 2012). This inherent uncertainty in blade pitch is thus expected to exert a certain degree of influence on wind turbine performance. To investigate the impact of blade pitch misalignment on the NTNU BT1 wind turbine's performance, Krogstad and Lund (2012) employed the BEM method and presented two figures for illustrative purposes, as depicted in Fig. 22. The results indicate that angle misalignment significantly affected the C_T values, particularly in the high *TSR* region. However for the C_P curves as shown in Fig. 22, it can be observed that it is less sensitive to the variation of blade pitch angle. These reported findings are consistent with the results shown in Fig. 21.

5. Conclusion

The overset-grid technique is widely considered to be the most theoretically correct and suitable approach for conducting CFD simulations of wind turbines. However, it should be noted that the predicted results obtained using this technique are sensitive to a plethora of numerical settings, including grid spacing, time increment, turbulence models, among others. Consequently, the systematic quantification of numerical uncertainties is essential in obtaining credible solutions from these simulations. In light of this, the objective of the present study is to develop a systematic and accessible procedure for obtaining reliable numerically predicted turbine performance from CFD simulations using overset grids. By identifying the most significant sources of uncertainty and their impact on the simulation results, this procedure aims to provide a comprehensive framework for quantifying numerical uncertainties while enhancing the accuracy and robustness of the predicted wind turbine performance.

Due to the fact that the blades of the target wind turbine were designed based on the NREL S826 airfoil, in order to ensure the accuracy and reliability of the CFD simulations of the wind turbine, preliminary simulations were carried out using FANS with overset grids for the NREL S826 airfoil experiment prior to conducting full turbine simulations. In order to verify the reliability of the CFD code FANS along with its overset-grid capability, the pressure distribution on the surface of the NREL S826 airfoil obtained from these simulations was compared against measured data. The comparative analysis revealed that the CFD code, FANS, used in the present study is able to accurately predict the pressure distribution on the airfoil surface.

The performance of the NTNU Blind Test 1 wind turbine was analyzed using the CFD code FANS with overset grids. To assess the accuracy and reliability of the numerical predictions, a comprehensive verification study was conducted, aiming to quantify the discretization uncertainties in the CFD simulations. To initiate the verification study, a numerical database obtained by using different configurations of grid spacing and time increment was created. By comparing the CFD predictions obtained from various combinations of grid and time step sizes in this study with those reported in an earlier work by the authors (Ye et al., 2023a), we conclude that structured grids require fewer grid points than unstructured grids to accurately resolve the blade tip geometry. Subsequently, the verification procedure described earlier was utilized to assess the numerical uncertainties associated with spatial and temporal discretization errors in the CFD simulations conducted using FANS with overset grids. The final numerical uncertainties for C_T and C_P were determined to be 7.3% and 8.1%, respectively. Based on the extensive investigation of numerical uncertainties in the simulations of the NTNU BT1 wind turbine, we emphasize that conducting a thorough verification study addressing both spatial and temporal resolution is crucial in obtaining credible predictions from CFD simulations utilizing overset grids.

Subsequently, simulations were conducted over a range of *TSR* spanning from 2 to 12. The CFD predictions were then compared, accounting for the uncertainty ranges established earlier, against the measured data as well as to the results obtained from other representative numerical approaches. Regarding the power coefficient C_P, the CFD predictions exhibited reasonably good agreement with the measured data, with the experimental measurements falling within the numerical uncertainty bars across the entire *TSR* range. However, for the thrust coefficient C_T, significant deviations between the numerical results obtained from the simulations and the experimental data were identified in the high *TSR* region ($TSR \geqslant 10$). Notably, the prediction of C_T using other representative numerical methods also demonstrated a considerable scatter compared to that of C_P. To elucidate on these observations, potential factors contributing to the discrepancies in C_T were proposed and discussed. However, further investigations are also recommended to fully understand the discrepancies between the numerical results and the experimental data in the high *TSR* region.

CRediT authorship contribution statement

Maokun Ye: Writing – original draft, Visualization, Validation, Software, Methodology, Investigation, Formal analysis, Data curation, Conceptualization. **Yan Zhao:** Data curation, Investigation, Validation, Visualization. **Hamn-Ching Chen:** Writing – review & editing, Supervision, Formal analysis, Data curation. **Decheng Wan:** Writing – review & editing, Supervision, Methodology, Investigation, Funding acquisition, Conceptualization.

Declaration of competing interest

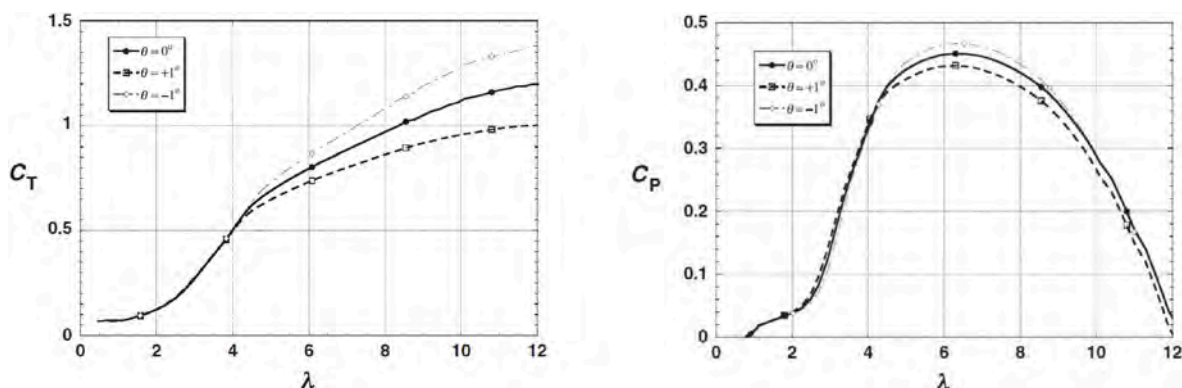The authors declare that they have no known competing financial

Fig. 22. Investigation of blade pitch misalignment, adopted from (Krogstad and Lund, 2012).

interests or personal relationships that could have appeared to influence the work reported in this paper.

Data availability

Data will be made available on request.

Acknowledgement

References

Bartl, J., Sagmo, K.F., Bracchi, T., Sætran, L., 2019. Performance of the nrel s826 airfoil at low to moderate Reynolds numbers—a reference experiment for cfd models. Eur. J. Mech. B Fluid 75, 180–192.

Bouras, I., Ma, L., Ingham, D., Pourkashanian, M., 2018. An improved k–ω turbulence model for the simulations of the wind turbine wakes in a neutral atmospheric boundary layer flow. J. Wind Eng. Ind. Aerod. 179, 358–368.

Breton, S.P., Sumner, J., Sørensen, J.N., Hansen, K.S., Sarmast, S., Ivanell, S., 2017. A survey of modelling methods for high-fidelity wind farm simulations using large eddy simulation. Phil. Trans. Math. Phys. Eng. Sci. 375, 20160097.

Burmester, S., Vaz, G., el Moctar, O., 2020. Towards credible CFD simulations for floating offshore wind turbines. Ocean Eng. 209, 107237.

Calaf, M., Meneveau, C., Meyers, J., 2010. Large eddy simulation study of fully developed wind-turbine array boundary layers. Phys. Fluid. 22, 015110.

Celik, I.B., Ghia, U., Roache, P.J., Freitas, C.J., 2008. Procedure for estimation and reporting of uncertainty due to discretization in CFD applications. Journal of fluids Engineering-Transactions of the ASME 130, 078001.

Chen, H., 1989. The flow around wing-body junctions. In: Proc. 4th Symp. Num. Phys. Aspects Aerodyn. Flows, Cebeci ed. Long Beach, CA.

Chen, C.J., Chen, H.C., 1984. Finite analytic numerical method for unsteady two-dimensional Navier-Stokes equations. J. Comput. Phys. 53, 209–226.

Chen, H.C., Chen, C.R., 2023. Cfd simulation of a container ship in random waves using a coupled level-set and volume of fluid method. J. Hydrodyn. 1–10.

Chen, H.C., Patel, V.C., 1988. Near-wall turbulence models for complex flows including separation. AIAA J. 26, 641–648.

Chen, H.C., Patel, V.C., Ju, S., 1990. Solutions of Reynolds-averaged Navier-Stokes equations for three-dimensional incompressible flows. J. Comput. Phys. 88, 305–336.

Choi, N.J., Nam, S.H., Jeong, J.H., Kim, K.C., 2013. Numerical study on the horizontal axis turbines arrangement in a wind farm: effect of separation distance on the turbine aerodynamic power output. J. Wind Eng. Ind. Aerod. 117, 11–17.

de Jong Helvig, S., Vinnes, M.K., Segalini, A., Worth, N.A., Hearst, R.J., 2021. A comparison of lab-scale free rotating wind turbines and actuator disks. J. Wind Eng. Ind. Aerod. 209, 104485.

Draper, M., Guggeri, A., Mendina, M., Usera, G., Campagnolo, F., 2018. A large eddy simulation-actuator line model framework to simulate a scaled wind energy facility and its application. J. Wind Eng. Ind. Aerod. 182, 146–159.

Duque, E., Van Dam, C., Hughes, S., 1999. Navier-stokes Simulations of the Nrel Combined Experiment Phase Ii Rotor. 37th Aerospace Sciences Meeting and Exhibit, p. 37.

Eça, L., Hoekstra, M., 2009. Evaluation of numerical error estimation based on grid refinement studies with the method of the manufactured solutions. Comput. Fluid 38, 1580–1591.

Eça, L., Hoekstra, M., 2014. A procedure for the estimation of the numerical uncertainty of cfd calculations based on grid refinement studies. J. Comput. Phys. 262, 104–130.

Eça, L., Vaz, G., Toxopeus, S., Hoekstra, M., 2019. Numerical Errors in Unsteady Flow Simulations. In: Journal of Verification, Validation and Uncertainty Quantification, vol. 4.

Fang, Y., Duan, L., Han, Z., Zhao, Y., Yang, H., 2020. Numerical analysis of aerodynamic performance of a floating offshore wind turbine under pitch motion. Energy 192, 116621.

Feliciano, J., Cortina, G., Spear, A., Calaf, M., 2018. Generalized analytical displacement model for wind turbine towers under aerodynamic loading. J. Wind Eng. Ind. Aerod. 176, 120–130.

Ghandour, A., De Troyer, T., Runacres, M.C., 2022. A combined potential flow–bem model to study the tower shadow effect in wind turbines. J. Wind Eng. Ind. Aerod. 229, 105131.

Huang, H., Chen, H.C., 2021. Coupled cfd-fem simulation for the wave-induced motion of a calm buoy with waves modeled by a level-set approach. Appl. Ocean Res. 110, 102584.

Huang, H., Gu, H., Chen, H.C., 2022. A new method to couple fem mooring program with cfd to simulate six-dof responses of a moored body. Ocean Eng. 250, 110944.

Kim, H.S., Chen, H.C., Briaud, J.L., 2022. Numerical simulation of scour hole backfilling in unidirectional flow. J. Hydraul. Eng. 148, 04022013.

Krogstad, P.Å., Eriksen, P.E., 2013. "blind test" calculations of the performance and wake development for a model wind turbine. Renew. Energy 50, 325–333.

Krogstad, P.Å., Lund, J., 2012. An experimental and numerical study of the performance of a model turbine. Wind Energy 15, 443–457.

Krogstad, P.Å., Eriksen, P., Melheim, J., 2011. Blind Test Workshop: Calculations for a Model Wind Turbine. In: Summary Report, vol. 10.

Launder, B.E., Sharma, B.I., 1974. Application of the energy-dissipation model of turbulence to the calculation of flow near a spinning disc. Lett. Heat Mass Tran. 1, 131–137.

Launder, B.E., Spalding, D.B., 1983. The numerical computation of turbulent flows. In: Numerical Prediction of Flow, Heat Transfer, Turbulence and Combustion, pp. 96–116.

Li, Y., Paik, K.J., Xing, T., Carrica, P.M., 2012. Dynamic overset cfd simulations of wind turbine aerodynamics. Renew. Energy 37, 285–298.

Liu, Y., Xiao, Q., 2019. Development of a fully coupled aero-hydro-mooring-elastic tool for floating offshore wind turbines. J. Hydrodyn. 31, 21–33.

Liu, Y., Xiao, Q., Incecik, A., Peyrard, C., Wan, D., 2017. Establishing a fully coupled cfd analysis tool for floating offshore wind turbines. Renew. Energy 112, 280–301.

Lynch, C., Smith, M., 2013. Unstructured overset incompressible computational fluid dynamics for unsteady wind turbine simulations. Wind Energy 16, 1033–1048.

Make, M., Vaz, G., 2015. Analyzing scaling effects on offshore wind turbines using cfd. Renew. Energy 83, 1326–1340.

Mo, J.O., Choudhry, A., Arjomandi, M., Lee, Y.H., 2013. Large eddy simulation of the wind turbine wake characteristics in the numerical wind tunnel model. J. Wind Eng. Ind. Aerod. 112, 11–24.

Nilsson, K., 2015. Numerical Computations of Wind Turbine Wakes and Wake Interaction. Ph.D. thesis. KTH Royal Institute of Technology.

Nilsson, K., Ivanell, S., Hansen, K.S., Mikkelsen, R., Sørensen, J.N., Breton, S.P., Henningson, D., 2015. Large-eddy simulations of the lillgrund wind farm. Wind Energy 18, 449–467.

Plaza, B., Bardera, R., Visiedo, S., 2015. Comparison of bem and cfd results for Mexico rotor aerodynamics. J. Wind Eng. Ind. Aerod. 145, 115–122.

Pontaza, J., Chen, H., Reddy, J., 2005. A local-analytic-based discretization procedure for the numerical solution of incompressible flows. Int. J. Numer. Methods Fluid. 49, 657–699.

Roache, P.J., 2009. Fundamentals of Verification and Validation. hermosa publ.

Shen, W.Z., Sørensen, J.N., Mikkelsen, R., 2005. Tip loss correction for actuator/Navier–Stokes computations. J. Sol. Energy Eng. 127, 209–213.

Sørensen, J.N., Myken, A., 1992. Unsteady actuator disc model for horizontal axis wind turbines. J. Wind Eng. Ind. Aerod. 39, 139–149.

Sorensen, J.N., Shen, W.Z., 2002. Numerical modeling of wind turbine wakes. J. Fluid Eng. 124, 393–399.

Thé, J., Yu, H., 2017. A critical review on the simulations of wind turbine aerodynamics focusing on hybrid rans-les methods. Energy 138, 257–289.

Tian, W., Zheng, K., Hu, H., 2021. Investigation of the wake propagation behind wind turbines over hilly terrain with different slope gradients. J. Wind Eng. Ind. Aerod. 215, 104683.

Tran, T.T., Kim, D.H., 2016a. A cfd study into the influence of unsteady aerodynamic interference on wind turbine surge motion. Renew. Energy 90, 204–228.

Tran, T.T., Kim, D.H., 2016b. Fully coupled aero-hydrodynamic analysis of a semi-submersible fowt using a dynamic fluid body interaction approach. Renew. Energy 92, 244–261.

Troldborg, N., 2009. Actuator Line Modeling of Wind Turbine Wakes. Ph.D. thesis. Technical University of Denmark.

Van Der Kolk, N.J., Akkerman, I., Keuning, J.A., Huijsmans, R.H.M., 2020. Part 2: simulation methodology and numerical uncertainty for RANS-CFD for the hydrodynamics of wind-assisted ships operating at leeway angles. Ocean Eng. 201, 107024.

Wang, Y., Chen, H.C., Vaz, G., Burmester, S., 2019. Cfd simulation of semi-submersible floating offshore wind turbine under pitch decay motion. In: International Conference on Offshore Mechanics and Arctic Engineering. American Society of Mechanical Engineers, V001T01A002.

Wang, Y., Chen, H.C., Koop, A., Vaz, G., 2021a. Verification and validation of cfd simulations for semi-submersible floating offshore wind turbine under pitch free-decay motion. Ocean Eng. 242, 109993.

Wang, Y., Chen, H.C., Vaz, G., Mewes, S., 2021b. Verification study of cfd simulation of semi-submersible floating offshore wind turbine under regular waves. In: International Conference on Offshore Mechanics and Arctic Engineering. American Society of Mechanical Engineers, V001T01A010.

Xie, S., Archer, C.L., 2017. A numerical study of wind-turbine wakes for three atmospheric stability conditions. Boundary-Layer Meteorol. 165, 87–112.

Ye, M., Chen, H.C., 2019. Viv Simulation of Riser-Conductor Systems Including Nonlinear Soil-Structure Interactions. In: Ocean Systems Engineering, vol. 9, pp. 241–259.

Ye, M., Chen, H.C., Koop, A., 2022. Comparison of different wind turbine modeling strategies in cfd simulations. In: The 32st International Ocean and Polar Engineering Conference, pp. 275–281. OnePetro.

Ye, M., Chen, H.C., Koop, A., 2023a. High-fidelity cfd simulations for the wake characteristics of the ntnu bt1 wind turbine. Energy 265, 126285.

Ye, M., Chen, H.C., Koop, A., 2023b. Verification and validation of cfd simulations of the ntnu bt1 wind turbine. J. Wind Eng. Ind. Aerod. 234, 105336.

Zahle, F., Sørensen, N.N., Johansen, J., 2009. Wind Turbine Rotor-Tower Interaction Using an Incompressible Overset Grid Method. In: Wind Energy: an International Journal for Progress and Applications in Wind Power Conversion Technology, vol. 12, pp. 594–619.

Zhang, R., Xin, Z., Huang, G., Yan, B., Zhou, X., Deng, X., 2022. Characteristics and modelling of wake for aligned multiple turbines based on numerical simulation. J. Wind Eng. Ind. Aerod. 228, 105097.